

Research



Article submitted to journal

Subject Areas:

xxxxx, xxxxx, xxxxx

Keywords:

Deep Learning, Machine Learning,
PET-CT, Skeletal Metastases,
Spectral Total-Variation, Radiomics

Author for correspondence:

Guy Gilboa

e-mail: guy.gilboa@ee.technion.ac.ilEnsemble of Weak Spectral
Total Variation Learners: a
PET-CT Case Study

Anna Rosenberg¹, John Kennedy², Zohar
Keidar³, Yehoshua Y. Zeevi⁴ and Guy
Gilboa⁵

¹srosnrg@campus.technion.ac.il²j_kennedy@rambam.health.gov.il³z_keidar@rambam.health.gov.il⁴zeevi@ee.technion.ac.il⁵guy.gilboa@ee.technion.ac.il

Solving computer vision problems through machine learning, one often encounters lack of sufficient training data. To mitigate this we propose the use of ensembles of weak learners based on spectral total-variation (STV) features (Gilboa 2014). The features are related to nonlinear eigenfunctions of the total-variation subgradient and can characterize well textures at various scales. It was shown (Burger et-al 2016) that, in the one-dimensional case, orthogonal features are generated, whereas in two-dimensions the features are empirically lowly correlated. Ensemble learning theory advocates the use of lowly correlated weak learners. We thus propose here to design ensembles using learners based on STV features.

To show the effectiveness of this paradigm we examine a hard real-world medical imaging problem: the predictive value of computed tomography (CT) data for high uptake in positron emission tomography (PET) for patients suspected of skeletal metastases. The database consists of 457 scans with 1524 unique pairs of registered CT and PET slices. Our approach is compared to deep-learning methods and to Radiomics features, showing STV learners perform best (AUC=0.87), compared to neural nets (AUC=0.75) and Radiomics (AUC=0.79). We observe that fine STV scales in CT images are especially indicative for the presence of high uptake in PET.

1. Introduction

Machine learning is highly instrumental in solving various computer vision tasks. Exceptional results are obtained when abundance of data exists for training. In some domains, however, labeled data for training is scarce, such as in detecting specific diseases based on medical imaging scans. A common practice to overcome data scarcity in (artificial) neural networks (NN's), is to use pre-trained models and transfer-learning approaches. However, the performance of such techniques is not always sufficient. Part of the problem is that the extracted features are of low relevance for the specific task at hand.

In this study we aim to examine the usability of features related to the total variation functional in the context of medical imaging, and specifically, for *computed tomography* (CT) analysis. Total variation (TV) has shown to be a high-quality regularizer in medical imaging applications, since it is edge preserving and promotes low-curvature shapes. To analyze features related to TV one can use the TV transform, or spectral TV [1–3]. To extract image features a (sub)-gradient flow with respect to the TV functional is evolved, initialized with the desired image. A spectral band is extracted by applying a second order numerical time-derivative, where time represents the spectral scale. It was shown that when the initial image is a solution of a nonlinear eigenvalue problem with respect to the TV subgradient (see examples in Fig. 1), a single response occurs at a time inversely proportional to the eigenvalue. In the general case, the image is decomposed into blob-like features at increasing scale, in an edge-preserving manner, as shown in Fig. 2. A comprehensive theory for this representation was established in [4]. A significant result is that the spectral responses at all scales are orthogonal to each other, in one-dimension, for any initial condition. Theoretical underpinning in the continuous case was further investigated in [4].

Our aim here is to design a robust classifier, based on STV features. We use an ensemble of weak classifiers, each based on different spectral bands. The low correlation of these features yields a very robust design. The classifier is applied to solve a hard real-world medical imaging problem. We attempt to use CT scans for the diagnosis of skeletal metastases. Labels are obtained from *positron emission tomography* imaging (PET). PET/CT registered images are used, where PET high-uptake serves as ground truth. We compare our method to Radiomics, common medical imaging features, and to deep neural networks in several configurations. The main contributions of this work are:

- (i) A general design is proposed for using ensemble classifiers based on spectral total-variation features.
- (ii) The advantages of this design are shown for the diagnosis of skeletal metastases from CT scans. This is a hard real-world classification problem. The proposed approach significantly outperforms common neural-network methods, as well as classical medical features, indicating that STV representation can be of high relevance.
- (iii) It is shown that fine scale textures, which can be well visualized by this approach, are of high significance for the classification problem.

2. Background

Positron emission tomography imaging (PET) with 18F-fluoro-2-deoxyglucose (FDG) has become a key method for imaging metabolism in order to detect pathological processes (e.g. cancerous sites) and healthy tissue (e.g. viable heart muscle). Hybrid PET/x-ray computed tomography (CT) examinations have become the main method in diagnosing skeletal metastases in cancer patients, but these dual imaging modalities expose patients to a larger dose of ionizing radiation than the CT scan itself. The aim of this study is to determine if machine learning methods can be used to extract features from the CT component of the PET/CT imaging that are useful for the diagnosis of skeletal metastases.



Figure 1. Examples of TV eigenfunctions. In \mathbb{R}^2 , indicator functions of convex sets, where the maximal curvature is below the area-perimeter ratio, are eigenfunctions with respect to the subdifferential of TV, admitting the nonlinear eigenvalue problem $\lambda u \in \partial J_{TV}(u)$. Spectral TV [3] approximates a decomposition of the signal into this type of structure at various scales.

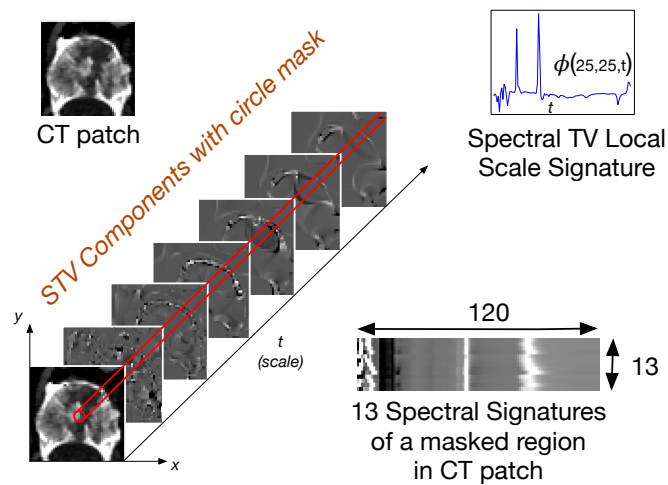


Figure 2. Feature Extraction Overview. Spectral TV transform is applied on a CT patch and 120 Spectral components are obtained. Each pixel at location (x, y) is described by a Spectral TV Local scale signature, $\phi(x, y, t)$. The signatures of 13 pixels that are inside the circular mask are used as features.

Positron emission tomography combined with computed tomography is used in nuclear medicine, particularly to detect cancerous processes. PET/CT imaging is acquired in the same scanner, during a single imaging session [5], and provides an accurately aligned scan of a high-resolution anatomic image from the CT and a functional image from the PET. The PET modality uses radioactive material that can be absorbed in cancer cells since they are in most of the cases more metabolically active in comparison to the surrounding healthy cells. PET imaging maps body metabolism and allows the detection of disease in its early stages, often before anatomical changes are evident. CT imaging by itself provides a high-resolution anatomic scan but does not give the metabolic information readily provided by PET [6].

Machine learning (ML) has been widely used in medical imaging over the past two decades. Examples of medical imaging tasks that are solved using machine learning are image segmentation, object detection, CAD diagnosis, classification, image registration, image reconstruction, image denoising and image synthesis. Deep learning approaches are commonly used in the medical image segmentation field. See for example, [7], [8], [9], [10], [11].

“Radiomics” enables high throughput features extraction from CT, MRI or PET images. The extracted data is analyzed for improving oncology patient diagnostic and clinical decision making [12]. There is active research on radiomics applied in the field of PET-CT imaging. Parmar et al. [13] compared ML approaches and methods of radiomics features selection from pre-treatment

CT images of lung cancer patients for achieving accurate and reliable survival prediction. Hsu et al. [14] introduces classifiers based on random forests and FDG-PET radiomics to distinguish normal tissue uptake from uptake in tumor. Bogowicz et al. [15] combined CT radiomics features of primary tumors and radiomics of lymph nodes detected by FDG-PET in order to improve loco-regional control prediction accuracy. Bibault et al. [16] used a DNN and pre-treatment radiomics features extracted from CT scan to predict the response after chemoradiation in locally advanced rectal cancer. In recent studies, combination of structural and functional radiomics was explored [17], for example PET/CT radiomics in [18], [19], [20], [21], [22].

Artificial intelligence has been applied to the skeletal metastases detection, segmentation, classification, and prognosis. Kairemo et al. [23] conducted a comparative study of PET/CT radiomics analysis for the assessment of the extent of active metastatic skeletal disease in prostate cancer. They concluded that CT alone cannot be used in this task. Yin et al. [24] developed MRI-based radiomics model for differentiation of three most common sacrum tumors. Naseri et al. [25] used planning-CT images of patients with non-metastatic lung cancer and patients with spinal bone metastases to evaluate various feature selection methods and machine learning classifiers for distinguishing between metastatic and healthy bone. Lang et al. presented a convolutional neural network (CNN) that differentiates metastatic lesions in the spine originated from primary lung cancer and other cancers using MRI images and radiomics analysis [26]. Filograna et al. showed the radiomics features extracted from MRI images of 8 oncological patients with bone marrow metastatic disease that is able to differentiate between metastatic and non-metastatic vertebral bodies [27]. Hinzpeter et al. studied the feasibility of differentiation of bone metastases not visible in CT from unaffected bone using [68Ga] Ga-PSMA PET imaging of 67 patients with prostate cancer as ground truth; They selected 11 radiomic features from CT images of 67 prostate cancer patients and trained a gradient-boosted tree to classify patients' bones into bone metastasis and normal bone, achieving accuracy of 0.85 [28]. Fan et al. [29] build classification models utilizing PET texture features to distinguished between benign vs. malignant bone lesions and showed that some texture features showed higher diagnostic value for spinal metastases than SUVmax.

The work of Ben-Cohen et al. [30] explored PET image synthesis using CT scans and deep learning networks. Their generated virtual PET images can be used for false-positive reduction in lesion detection solutions and may enable lesion detection in a CT-only environment. The lesion detection results were not demonstrated in that work.

Bi et al. [31] proposed a multi-channel generative adversarial network (M-GAN) for generating PET data. Their model takes the input from the given label and from the CT images, to synthesize the high uptake consistent with the anatomical information. They have shown that their generated PET images boost the training data for machine learning methods. To generate a synthetic PET image using Bi et al. [31] method, manual labeling of the tumors is required.

3. Spectral TV

In this work we examine the use of STV to provide indicative features for the complex task of uptake prediction based on CT data. STV is an edge-preserving nonlinear transform, introduced in [2,3] and employed for various image-processing tasks, such as image manipulation [32], segmentation [33], mesh-processing [34] and more [1]. In the context of medical imaging, it has been instrumental in image fusion [35,36]. The spectral signatures are used here for the first time as classification features. We summarize first the fundamental concept and properties of STV.

(a) Spectral Total Variation

Many studies have explored the application of linear models in image processing tasks. The Fourier transform has been the "workhorse" in signal filtering and representation since it is a mathematically simple, effective, and intuitive method. For real-world piecewise signal with edges this representation is less adequate. Therefore, modern algorithms tend to use nonlinear methods. Gilboa et al. have conducted research on nonlinear eigenvalue analysis and have

introduced a new approach of nonlinear multi-scale representation for image processing [1–3]. Let us first set up some notations, in order to explain this transform. The total-variation (TV) energy for smooth functions is

$$J_{TV}(u) = \int_{\Omega} |\nabla u(x)| dx. \quad (3.1)$$

The subgradient $p(u) \in \partial J_{TV}(u)$, where ∂J_{TV} denotes the subdifferential, is

$$p(u) = -\operatorname{div} \left(\frac{\nabla u}{|\nabla u|} \right). \quad (3.2)$$

This definition applies for smooth functions u with non-vanishing gradients and is also referred to as the (negative) 1-Laplacian. A more general definition for signals in the space of bounded variations BV can be found e.g. in [1,37]. The transform seeks a decomposition of a signal into elements which admit the following nonlinear eigenvalue problem,

$$\lambda u \in \partial J_{TV}(u).$$

It turns out that indicator functions of convex sets with low enough curvature (disk-like shapes) admit this eigenvalue problem [37], see Fig. 1. The decomposition of a signal $f(x) \in BV$ into spectral components is performed by evolving the total-variation gradient flow

$$\partial_t u(t, x) \in -\partial J(u(t, x)), \quad u(0, x) = f(x), \quad (3.3)$$

where ∂_t denotes the first partial derivative with respect to an artificial time parameter t . This parameter can be also interpreted as scale in nonlinear scale-space. The spectral component (i.e. the transform) of $f(x)$ at scale t is defined by

$$\phi(t, x) := t \partial_{tt} u(t, x), \quad (3.4)$$

where $u(t, x)$ is the solution of (3.3) and ∂_{tt} is the second order partial derivative w.r.t. t . In [4] the following key properties were shown:

- (i) A single eigenfunction with eigenvalue λ appears as a delta at scale $t = 1/\lambda$ in the transform domain.
- (ii) The reconstruction formula for decomposed data f is based on simple integration of the spectral components via

$$f = \int_0^\infty \phi(t) dt + \bar{f}, \quad (3.5)$$

where \bar{f} is the mean value of f .

- (iii) A spectrum is defined by

$$S(t) := \langle f, \phi(t) \rangle_{\Omega}, \quad (3.6)$$

which admits a Parseval-type identity, $\int_0^\infty S(t) dt = \|f\|_{L^2}^2$.

- (iv) Motivated by the reconstruction formula (3.5), filtering is formulated in an analogous manner to Fourier filtering via

$$f_H = \int_0^\infty H(t) \phi(t) dt + \bar{f}, \quad (3.7)$$

for a filter function H that can enhance, damp or remove certain frequencies.

We note that the above can be generalized beyond TV, for all norms and semi-norms in a discrete setting within Euclidean spaces or graphs. In a restricted setting, such as the discrete 1D case, it was shown in [4] that:

- (i) The spectral representations yield a decomposition of the input signal into eigenfunctions.

- (ii) Spectral components (which turns out to be a difference of two eigenfunctions) are pairwise orthogonal.

Additional details of the transform and its implementations can be found in [1,3].

Computational considerations. We note that computing STV involves solving a nonlinear PDE (TV-flow) which requires some computational efforts. At each scale, the solution to the TV flow must be computed, involving solving multiple non-smooth optimization problems. This process can be computationally expensive. There are several studies which aim at considerably increasing the speed of these computations (by orders of magnitude), most notably by specific neural network architectures, see [38–40].

(b) Spectral TV Local Scale Signatures

Hait et al. [35] used STV to form a continuous, multi-scale, fully edge-preserving, and local descriptor, referred to as spectral total-variation local scale signatures. Given an image $f(x)$, we denote by $\phi_f(x, t)$ the respective STV spectral components, Eq. (3.4). A time-discrete setting of the TV gradient flow, (3.3), is solved. The evolution is for n iterations with time step Δt , reaching a maximal scale of $T = n \cdot \Delta t$. We thus obtain for each pixel a vector of n features, as shown in Fig. 2 top right. This feature vector (signature) can be viewed as the multiscale spectral response of the pixel. Several properties of these signatures were presented in [35]:

Sensitivity to size and to local contrast. Objects with different contrast and size have distinct signatures in their image. Spatial scaling and contrast change by a positive scalar a affect the signatures as follows,

$$\phi_{f(ax)} = a\phi_f(ax, at), \quad (3.8)$$

$$\phi_{af(x)} = \phi_f(x, t/a). \quad (3.9)$$

Invariance to Rotation, Translation, and Flip. The following invariances in \mathbb{R}^n were shown,

$$\phi_{f(Rx)} = \phi_f(Rx, t), \quad (3.10)$$

$$\phi_{f(x-a)} = \phi_f(x - a, t), \quad (3.11)$$

$$\phi_{f(x)}(x) = \phi_{f(-x)}(-x). \quad (3.12)$$

where R is a rotation matrix, and a is a spatial shift. Hait et al. presented several applications of the proposed framework, such as image clustering and fusion of thermal, optic, and medical images. To increase the distinctness of salient objects and to improve clustering, the following signature enhancement was proposed,

$$\Phi_f(x) = \phi(x, t) \cdot \|\phi(x, t)\|_{[0, T]}^p. \quad (3.13)$$

This enhancement follows the methodology introduced in [35], where each signature is “stretched” according to its L_p norm (commonly L_1), which strengthens and sparsifies the representation of salient structures. This process increases the separation between different features, thus improving distinctness and clustering performance.

4. Classification Method

We investigate a new method of diagnosing patients with skeletal metastases, based on CT imaging and STV, without PET metabolic function imaging. An STV transform of CT images allows extracting local descriptors that potentially uncover conspicuous pathology that may not be noticeable in the CT scan. The unique features at the locations of pathology were confirmed by the diagnostic readings of the PET radiotracer uptake.

The proposed method should enable the detection of pathology based on CT scans consistent with metabolic scans. It could as such aid in patient diagnosis and management. Our framework includes training and test modules. The training is performed using CT images and lesion labels

acquired through PET. The test process is based on CT images only, which may allow diagnosis in early stages of pathology.

We compare STV to radiomics features, both methods are followed by classical learning (based on decision trees). In addition, this study is complemented by examining deep neural networks which execute the same task. Since data is limited, to train neural networks in an optimal manner, transfer learning is used, as customary in such cases. Two pretrained networks were examined, based on natural images and on medical images. The training and testing sets for all methods were the same.

(a) PET/CT imaging and image acquisition

Patient scans were performed on a PET/CT system (Discovery 690, GE Healthcare, Waukesha, WI) combining a dedicated time-of-flight PET with a lutetium-yttrium oxyorthosilicate (LYSO) scintillator and a 64-slice CT. The institutional review board approved this retrospective study, waiving the requirement to obtain informed consent. After an intravenous injection of an activity of 5 MBq/kg FDG, a 60 minute uptake period was followed by a PET acquisition of 1.5 minutes per bed position. Patient scans were reconstructed on a 256×256 matrix, with a 70 cm transverse field-of-view (FOV) and a 3.27 mm slice thickness using a 3D ordered subset expectation maximization (OSEM) algorithm (24 iterations, 2 subsets, 6.4 mm full width at half maximum Gaussian filter). The CT was acquired using a peak voltage of 120 kV, a pitch of 1.375, 0.7 s/rotation, and variable current (100 mA minimum, 650 mA maximum, noise index 11.57). CT images were reconstructed on a 512×512 matrix, with a 50 cm diameter transverse FOV and a 2.5 mm slice thickness using filtered backprojection and 40% adaptive statistical iterative reconstruction.

(b) Construction of experimental data set

We analyzed 457 patients: 249 oncological patients with confirmed bone metastases disease and 208 patients without metastases. Our focus was to examine the lower spine column. Among 249 oncological patients we identified 71 patients that were diagnosed with vertebral lesions in the lower spine column and included them in our study. Other oncological patients were identified with bone metastases not in the spine or not in the lower spine column. We then selected 71 healthy patients to be included in our study as a way of keeping a balanced number of pathological and healthy patients. In total, our model was built on 142 patients with 71 lesions in the lower spine and 71 without lesions.

From 71 pathological patients we extracted 613 patches of lower spine with high uptake regions and 298 patches of lower spine with low uptake regions. From 71 healthy patients we extracted 613 patches of the lower spine. To reduce the imbalance we used the low uptake patches of pathological patients twice, so in total we used 1822 (1524 unique) two-dimensional patches for building our framework (613 patches with high uptake, 596 patches from pathological patients with low uptake, 613 patches of healthy patients).

(c) Data pre-processing

Our data set includes a set of PET/CT 3D volumes of patients diagnosed with skeletal metastases and PET/CT 3D volumes of healthy patients. In order to obtain a 3D spine mask of each 3D CT volume, we utilized the spine segmentation methodology of Khandelwal et al. [41]. Using the obtained 3D spine mask and morphological operations, we extracted CT patches of vertebrae from the lower spine column, obtaining CT patches of 5 lumbar vertebrae (L1-L5) and last thoracic vertebra (T12). From each vertebra we extract up to 6 patches. An example of vertebra segmentation is shown in Fig. 3. The extracted patches' size was 50×50 pixels and a center of a patch was from the center of a vertebra's body. The obtained patches were manually examined, and if a patch did not include the vertebra due to incorrect segmentation, it was removed from

the data set. For each patch in the obtained data set, we extracted the registered PET patch from the corresponding PET volume.

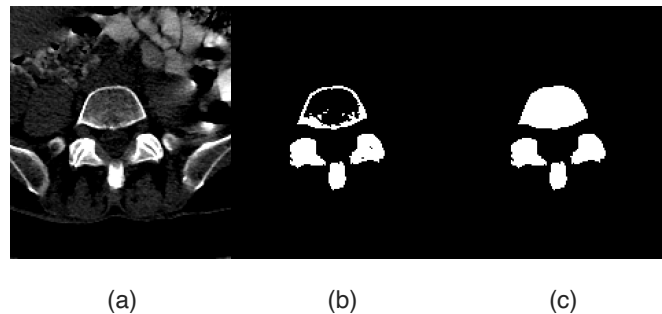


Figure 3. Segmentation of a vertebra patch. (a) CT image. (b) Slice from a 3D binary mask obtained with a sparse field method [42]. (c) The holes in the binary mask (b) are filled using a flood-fill algorithm.

(d) Data labeling

Each patient in the data set was labeled by a certified specialist nuclear medicine physician, providing a data-set with studies labeled as “Normal” and “Pathological”. All patches that were extracted from the normal studies were labeled as “Normal”. We used a set of PET patches from our pre-processed data set to label CT patches that were extracted from the pathological studies. We applied a circular mask of 13 pixels around the center of each PET/CT patch. In cases where the PET patch displayed a high uptake within the circular mask, we labeled the CT patch as “Pathological High Uptake (HU)”, otherwise we labeled them as “Pathological Low Uptake (LU)”. From 71 pathological patients, we extracted 613 patches labeled as “Pathological High Uptake (HU)” and 298 patches labeled as “Pathological Low Uptake (LU).” From 71 healthy patients, we extracted 613 patches labeled as “Normal.”

(e) Proposed framework

After applying the spectral TV transform on a CT patch, using a signature enhancement with $p = 1$ (Eq. (3.13)), we obtain 120 STV components of a patch. We selected $p = 1$ for signature enhancement following the methodology proposed in [35], where it was shown to improve distinctness and sparsity of salient structures. Examples of distinctness of different spectral signatures (non-enhanced and enhanced) coming from one CT patch are presented in Fig. 4. Enhanced spectral signatures extracted from normal and pathological CT patches are presented in Fig. 5. We then apply a circular mask of 13 pixels around the center of each component, and use the obtained circles as input to the proposed framework. Every 5 adjacent components are considered a band, producing 24 bands in total, see Fig. 2. We rely on the fact that the spectral bands are lowly correlated. Theoretically, in 1D we obtain precise orthogonality and in 2D and higher dimensions this orthogonality is still an open problem, however numerically we observe lowly correlated bands [1]. For visualization purposes we present the normal and pathological first 6 bands in Fig. 6.

The model is composed of 24 decision trees, where each tree is trained using its associated band of features. For example, the decision tree number 1 was trained using the feature band number 1, which included scales from 1 to 5, the decision tree number 2 was trained using the feature band number 2, which included scales from 6 to 10, etc. Each decision tree was trained using MATLAB’s `fitctree` function with default hyperparameters, and was tasked with classifying

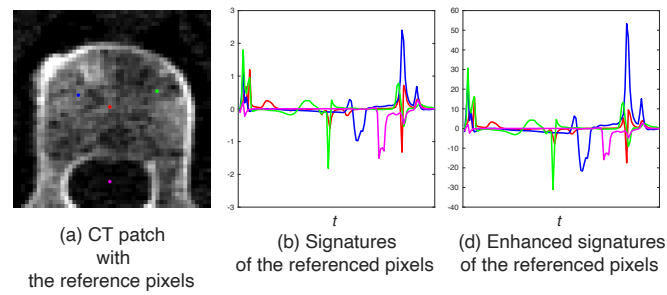


Figure 4. Distinctness of signatures of the referenced pixels.

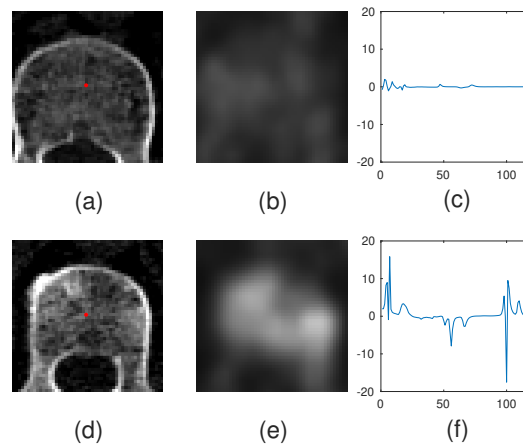


Figure 5. Example of CT and PET patches and signature of the referenced pixel (red). (a) Normal CT patch with referenced pixel. (b) Normal PET patch. (c) Normal spectral TV local scale signature of referenced pixel in CT patch (red). (d) Pathological CT patch with reference pixel. (e) Pathological PET patch. (f) Pathological spectral TV local scale signature of referenced pixel in CT patch.

the signature's band into 3 classes i.e., "Pathological High Uptake", "Pathological Low Uptake", and "Normal". Each pixel was characterized by 24 bands, that is, the framework generated 24 tags for each pixel. Our purpose is to reveal high uptake regions. Thus, after each pixel was classified with 24 tags, the "Pathological Low Uptake" tags were changed with the tag "Normal" to convert the problem into a binary classification problem. The prediction score of the pixel was obtained by calculating the mean of 24 tags that were associated with the pixel. Averaging the pixels' scores of a patch, provided a patch score. Each vertebra consisted of at most 6 patches, that is, the vertebrae's score was obtained by averaging its patches scores. If at least one vertebrae score was higher than a predefined cutoff the study was classified as "Pathological". Our train and test flowcharts for decision trees based model are presented in Fig. 7 and Fig. 8.

Trying to enhance the quality of the results we also utilized the random forest algorithm per each band of features. We generated 24 random forests and each forest was trained on a different band of features. In the results section we can observe that the use of random forest, in this case, is not essential.

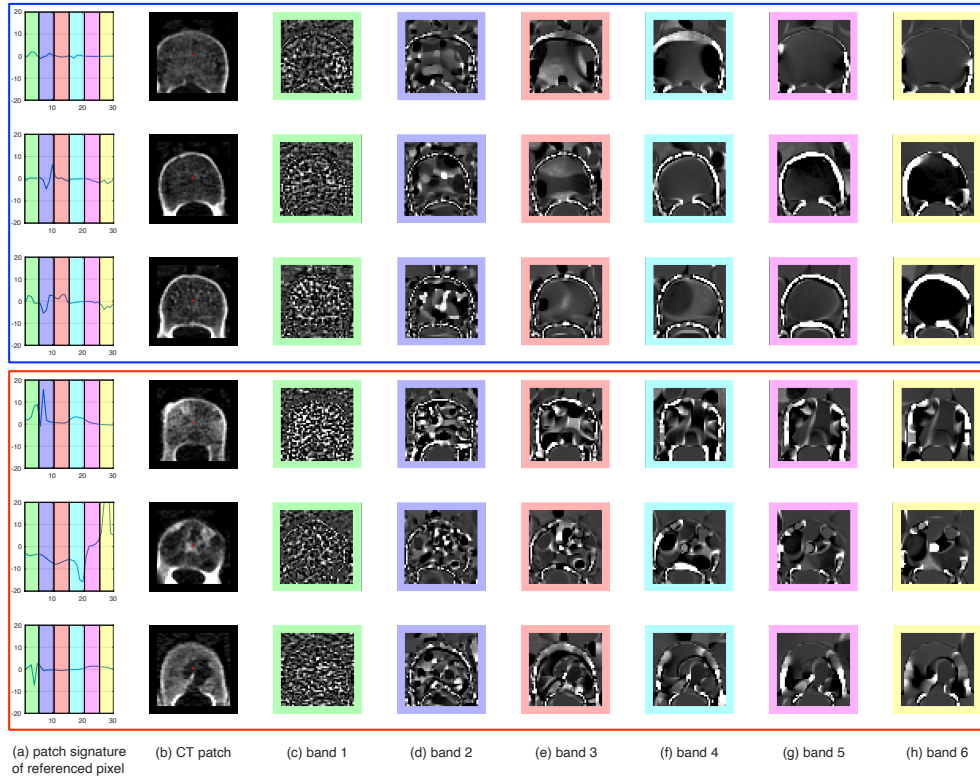


Figure 6. Visual demonstration and comparison of normal and pathological bands. Normal examples are shown in the blue frame. Pathological examples are shown in the red frame.

Algorithm 1 Algorithm for Patient Diagnosis

```

1: for Every fold do
2:    $X_{test} \leftarrow fold_i$  ▷ Keep the current fold as a hold-out
3:    $X_{train} \leftarrow remaining\ folds$  ▷ Use the remaining folds as a training data-set
4:   for Every feature band do
5:      $X_{train\_band} \leftarrow X_{test}(feature\ band_j)$ 
6:      $fit(X_{train\_band})$  ▷ Fit the model on the features band from the training data set
7:      $X_{test\_band} \leftarrow X_{test}(feature\ band_j)$ 
8:      $Y_{test\_predicted\_band} = predict(X_{test\_band})$ 
9:     ▷ Test the model on the features band from the hold out fold
10:     $Y_{test\_predicted} = [Y_{test\_predicted}\ Y_{test\_predicted\_band}]$  ▷ Retain the prediction results
11:   end for
12: end for
13: for Every patient do
14:   for Every low back vertebra do
15:     Calculate vertebra mean prediction  $P_{v_i}$ 
16:     if  $P_{v_i} > cutoff$  then
17:       Label patient as "Pathological"
18:     end if
19:   end for
20: end for

```

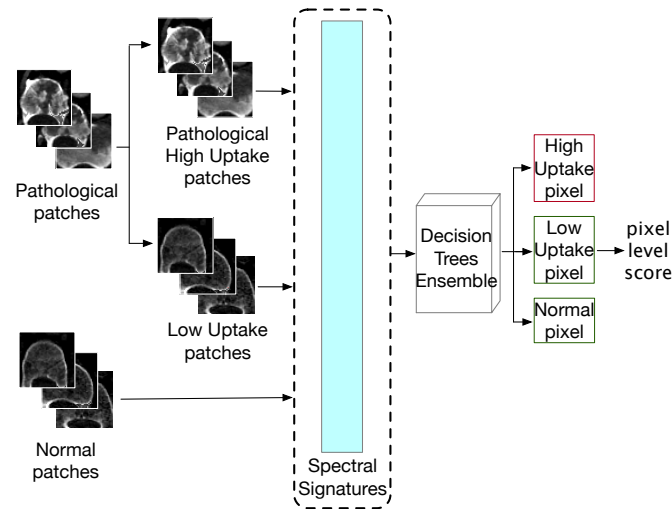


Figure 7. Overview of the training procedure for pixel level prediction. First Spectral signatures were obtained by applying STV transform on the input CT patches. The spectral signatures of the pixels inside the circle mask were deployed as features for training Decision Tree Ensemble, which generates 3-class labels. The "Low Uptake" label was replaced with the "Normal" label, and the pixel level score was calculated.

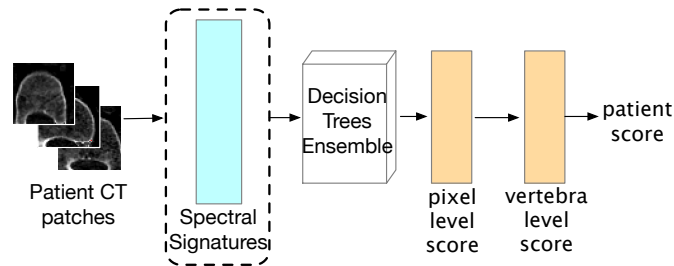


Figure 8. Overview of the testing procedure for patient level prediction. First Spectral signatures were obtained by applying STV transform on the input CT patches. The spectral signatures of the pixels inside the circle mask were deployed as features for testing Decision Tree Ensemble, which generates 3-class labels. The "Low Uptake" label was replaced with the "Normal" label, and the pixel level score was calculated. The vertebra score was calculated by averaging pixels' scores that belong to one vertebra. The patient is labeled as "Pathological" if he has at least one vertebra with a score higher than some predefined threshold.

Our algorithm can be interpreted as an ensemble method, where for each patch we have an ensemble of size 24. Since the bands are lowly correlated, the ensemble members produce diverse predictions, yielding a very powerful classifier that can accommodate well noisy and unreliable data. As we see later in the experimental section, this is a hard classification problem and the theoretical knowledge on STV affords a considerable improvement over generic methods.

(f) Ablation study

In the ablation study, we changed the number of adjacent components (scales) that were united into each band. We thereby changed the total number of bands. The ablation study was performed

on more restricted dataset that included 57 healthy patients without lesions and 57 pathological patients with confirmed lesions in the lower spine column. Different values of the adjacent components per band and the matching results are shown in Table 2.

Table 1. Performance Comparison, 10 Fold Cross Validation

Classification Method	AUC	Other Metrics			
		Accuracy	Specificity	Recall	Precision
Decision Trees Ensemble (ours)	0.87±0.01	0.80±0.01	0.84±0.04	0.77±0.04	0.83±0.03
Random Forests Ensemble (ours)	0.87±0.01	0.80±0.01	0.83±0.04	0.77±0.05	0.82±0.02
Random Forest, Spectral TV features	0.67±0.03	0.65±0.02	0.69±0.05	0.60±0.05	0.66±0.03
Random Forest, Radiomics Features	0.79±0.01	0.73±0.01	0.71±0.05	0.75±0.05	0.73±0.02
Random Forest Ensemble, Radiomics Features	0.79±0.004	0.74±0.01	0.68±0.01	0.81±0.02	0.71±0.01
Transfer Learning ResNet-50, ImageNet [43], freezeall	0.60±0.01	0.62±0.02	0.45±0.07	0.78±0.07	0.59±0.01
Transfer Learning ResNet-50, ImageNet [43], unfreetop10	0.62±0.05	0.62±0.04	0.64±0.12	0.61±0.12	0.63±0.04
Transfer Learning ResNet-50, ImageNet [43], additional layers	0.70±0.02	0.68±0.02	0.61±0.06	0.75±0.04	0.66±0.03
Transfer Learning ResNet-50, RadImageNet [44], freezeall	0.75±0.01	0.69±0.01	0.75±0.09	0.64±0.08	0.73±0.05
Transfer Learning ResNet-50, RadImageNet [44], unfreetop10	0.68±0.02	0.65±0.02	0.82±0.17	0.48±0.18	0.79±0.13
Transfer Learning ResNet-50, RadImageNet [44], additional layers	0.68±0.02	0.66±0.01	0.75±0.12	0.56±0.12	0.70±0.06

Table 2. Ablation Study, 10 Fold Cross Validation

Classification Method	Scales per tree	Correlated	Metric					
			Cutoff	Accuracy	Specificity	Recall	Precision	AUC
Decision Trees Ensemble	3	No	0.45	0.78	0.84	0.72	0.82	0.84
Decision Trees Ensemble	4	No	0.45	0.79	0.74	0.84	0.76	0.86
Decision Trees Ensemble	5	No	0.45	0.81	0.76	0.86	0.78	0.87
Decision Trees Ensemble	6	No	0.45	0.79	0.76	0.82	0.77	0.86
Decision Trees Ensemble	8	No	0.5	0.78	0.9	0.66	0.87	0.86
Decision Trees Ensemble	10	No	0.5	0.76	0.86	0.66	0.82	0.84
Decision Trees Ensemble	12	No	0.5	0.77	0.84	0.7	0.81	0.83
Decision Trees Ensemble	15	No	0.5	0.7	0.76	0.64	0.73	0.79
Decision Trees Ensemble	3	Yes	0.5	0.7	0.5	0.9	0.6428	0.8
Decision Trees Ensemble	4	Yes	0.5	0.69	0.48	0.9	0.63	0.79
Decision Trees Ensemble	5	Yes	0.55	0.72	0.72	0.72	0.72	0.8
Decision Trees Ensemble	6	Yes	0.5	0.69	0.48	0.9	0.63	0.79
Decision Trees Ensemble	8	Yes	0.5	0.69	0.48	0.9	0.63	0.79
Random Forests Ensemble	5	No	0.5	0.81	0.8	0.82	0.8	0.87
Random Forests Ensemble	6	No	0.5	0.75	0.68	0.82	0.72	0.85
Random Forests Ensemble	3	Yes	0.75	0.7	0.82	0.58	0.76	0.77
Random Forests Ensemble	5	Yes	0.75	0.7	0.82	0.58	0.76	0.77
Random Forest	120	N.A.	0.9	0.61	0.6	0.62	0.6	0.61

5. Results

Our proposed model was trained and validated using a 10-fold cross-validation technique. The validation was done on the out-of-fold patients, that is, on patients that were not used to train the model. We evaluated the proposed framework for validation via area under curve (AUC) of the receiver operating characteristic (ROC). Table 1 shows that the AUC of the proposed framework yields over 0.87. To avoid class imbalance, we selected a similar number of CT patches from different classes.

To investigate the importance of each decision tree in the ensemble, we exclude one decision tree and evaluated the performance in terms of AUC, based on the other 23 trees. The AUC drop is shown in Fig. 9). This experiment shows that trees that are built based on fine scale features are generally contributing more to the framework's performance. Interestingly, we also observed that the exclusion of certain trees led to an increase in AUC, particularly starting from band number 17

(corresponding to STV components from 81 onward). Additionally, we systematically examined the impact of the number of STV components used in the classification. We varied the number of components from 20 to 120 in steps of 10 and measured the corresponding AUC. The results, presented in Fig. 10, show that using 80 STV components yielded the highest AUC (0.88), slightly outperforming the 120-component configuration (0.87). This finding aligns with our tree exclusion analysis, suggesting that some higher-band STV components may introduce noise rather than useful information.

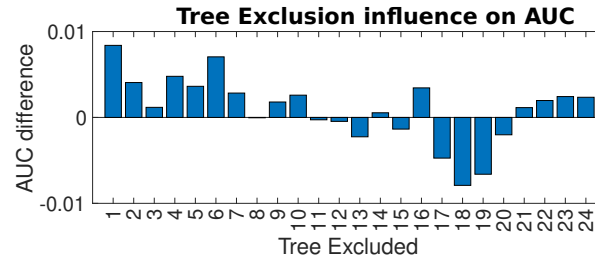


Figure 9. Band importance. In this experiment we attempt to assess the importance of each band for the final classification. This is done by excluding the tree corresponding to a band (out of 24 bands) and using the other 23 bands only for classification. We show the AUC drop compared to the AUC of using all bands $AUC_{orig} - AUC_{exc-band}$ (positive means the band is contributing positively). Trees associated with finer scales are generally more important for the final classification results.

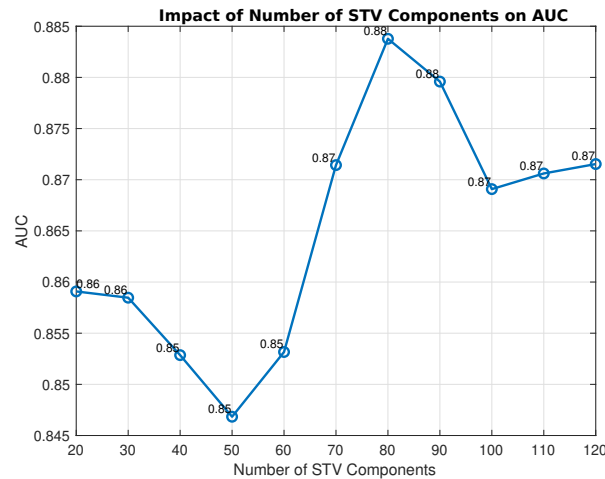


Figure 10. The impact of the number of STV components. The classifier's performance, measured by AUC, as a function of the number of STV components used in the classification task.

To explore a generic learning approach for classification, the random forest (RF) model was built based on all 120 STV components. Here we do not use ensembles and do not incorporate our prior knowledge on STV's low correlated nature. The performance thus drops sharply, where the RF algorithm yields the AUC value of 0.67. We did not evaluate boosting-based classifiers in this

study. Investigating whether boosting methods could further improve classification performance is a promising direction for future work.

To further motivate the choice of decision trees, we also evaluated a simple multi-layer perceptron (MLP) model directly on the spectral signatures. This model, which included three hidden layers with 15, 10, and 5 neurons respectively, achieved an AUC of only 0.63, substantially lower than our proposed framework.

Next, we compared our proposed framework to the radiomics features based model. In order to extract radiomics features from the CT patches, we used the open-source PyRadiomics package [45]. From each CT patch, we extracted 93 radiomics features (18 first order, 24 gray level co-occurrence matrix (GLCM), 14 gray level dependence matrix (GLDM), 16 gray level run length matrix (GLRLM), 16 gray level size zone matrix (GLSZM), 5 neighbouring gray tone difference matrix (NGTDM) features), using the same circle mask. Similarly to our method, we used 10 fold cross validation to train and evaluate random forest classifier based on the extracted radiomics features. The yielded AUC value is 0.79, the results are presented in table 1.

To compare our framework to DNN's, we used pre-trained ResNet-50 architecture [46]. We classified CT patches from our dataset into 3 classes ("Pathological HU", "Pathological LU", and "Normal"), using the ResNet-50 model, which was pre-trained on the ImageNet dataset [43]. To fine-tune the ResNet-50 architecture three methods were examined. In the first method, all layers were frozen. In the second method, we unfroze the last 10 layers. In the first and second methods, after the last pre-trained layer we added a global average pooling layer, a dropout layer, and an output layer activated by the softmax function to get the list of prediction scores. In the third method, we unfroze 2 last convolution blocks of ResNet-50 architecture for training, and then fed the extracted features into 2 fully connected dense layers with a rectified linear unit (ReLU) activation function and dropout regularization. To obtain the final 3 class probabilities we used a dense layer with the softmax activation function (see Fig. 11).

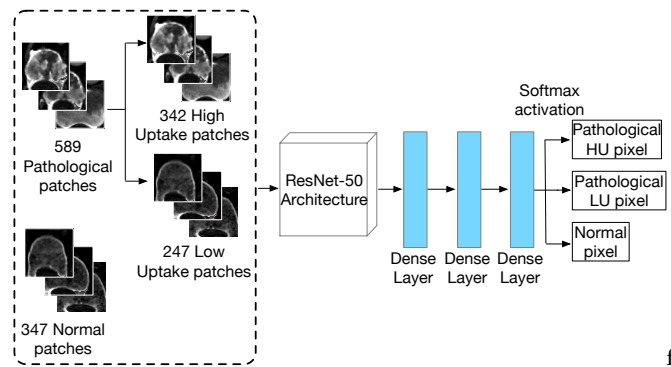


Figure 11. Overview of training procedure based on ResNet-50 architecture. Transfer learning method was utilized to extract features from pre-trained ResNet-50 model.

After classifying CT patches into 3 classes, in all three methods, we changed the "Pathological LU" obtained tags with the "Normal" tags. We then calculated the mean prediction of each vertebra. If at least one vertebra score was higher than a predefined cutoff, we classified the study as "Pathological". We evaluated the ResNet-50 based framework using the 10-fold cross-validation technique. Table 1 shows the AUC of the ResNet-50 based framework, for which the best option (third method above) reaches an AUC of 0.70.

Pretraining on ImageNet is most adequate for natural images and may not yield the best features for medical imaging. We thus utilized RadImageNet [44] which is intended specifically to be used on radiological data. A pre-trained model with ResNet-50 architecture is used, in order to improve the performance of the DNN-based framework. We trained three DNNs, in the same

way we trained ImageNet based models, the first one by freezing all layers, the second one by unfreezing last 10 layers, the third one by unfreezing 2 layers and adding 2 fully connected layers with (ReLU) activation function and dropout regularization, then an output fully connected layer with the softmax activation function. We achieved AUC of 0.75 by freezing all layers, the results are shown in table 1. In Fig. 12 we show the receiver operating characteristic (ROC) curves for two our models (the best performance), the random forest model based on radiomics features (a good performance), the ResNet-50 model based on the RadImageNet pre-trained weights (a good performance), the ResNet-50 model based on the ImageNet pre-trained weights (a poor performance).

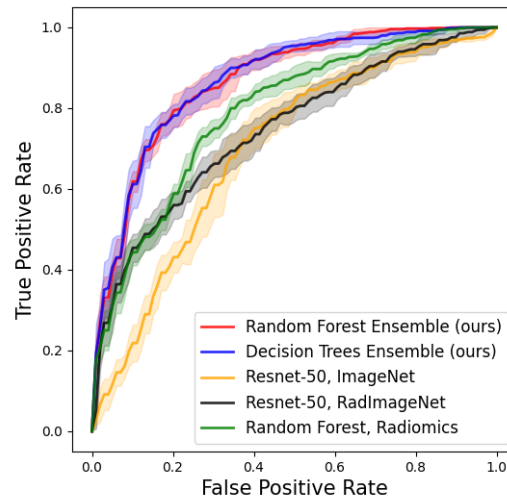


Figure 12. Patients classification results evaluated using mean receiver operating characteristic curve (ROC) with variability.

In Fig. 13 the mean spectrum (spectral response) $S(t)$ of patches' regions of interest is plotted. Mean spectral response of high uptake regions are higher than the mean spectral response of normal regions in almost all scales ($t \in [8, 120]$). This may explain the success of STV-based classification results. The code and the datasets are available at [Project Repository](#).

6. Discussion and Conclusion

We developed a novel classification model for differentiating pathological patients with skeletal metastases using CT scans, where PET information serves as ground truth in the training phase. Our model utilizes spectral TV signatures that were not used before in medical image classification, in general, and in bone metastases detection, in particular. In a standard procedure, radiologists diagnose skeletal metastases using PET/CT scans. Our approach opens ways to predict cases suspected of skeletal metastases based on CT only. This may enable early detection of metastases, as CT scanners are often more widely available. We investigated the ability to distinguish lesion bones from healthy bones. Our work demonstrates that spectral TV carries informative features for this task.

This is a hard classification problem, as there is strong variability in the data and the CT cues are subtle. We compared our results to radiomics features and to DNN based methods. Our method yields superior performance in terms of accuracy and AUC. Spectral TV (STV) signatures

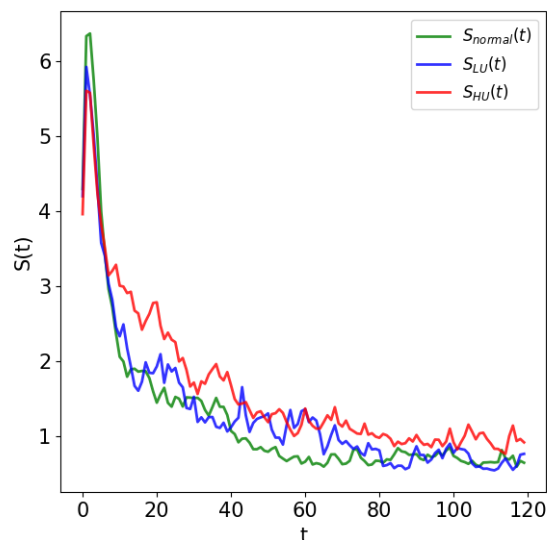


Figure 13. Mean spectral response $S(t)$, Eq. (3.6), of "Normal", "Low Uptake" (LU), and "High Uptake" (HU) regions. HU regions have higher mean spectral response $S(t)$ in almost every scales ($t \in [8, 120]$), most notably in the range $[10, 40]$. Pathological low-uptake has also a different mean spectral response, compared to normal patients.

[35] contain scale and space information that well differentiates objects of different contrast, size and structure. The lowly-correlated band characteristics allows to construct excellent ensembles that are resilient to noise and variability. In this study, we combined STV signatures into bands to form an ensemble of decision trees or random forests for classifying CT data. In ensemble learning, it is well known that most of the gain is obtained when the ensemble members are lowly correlated. Thus STV fits very well the ensemble framework, obtaining in each band different structural information. We believe additional classification tasks in CT and in medical imaging in general can benefit by the use of STV features.

References

1. Guy Gilboa.
Nonlinear eigenproblems in image processing and computer vision.
Springer, 2018.
2. Guy Gilboa.
A spectral approach to total variation.
In *Scale Space and Variational Methods in Computer Vision: 4th International Conference, SSVM 2013, Schloss Seggau, Leibnitz, Austria, June 2-6, 2013. Proceedings 4*, pages 36–47. Springer, 2013.
3. Guy Gilboa.
A total variation spectral framework for scale and texture analysis.
SIAM journal on Imaging Sciences, 7(4):1937–1961, 2014.
4. Martin Burger, Guy Gilboa, Michael Moeller, Lina Eckardt, and Daniel Cremers.
Spectral decompositions using one-homogeneous functionals.
SIAM Journal on Imaging Sciences, 9(3):1374–1408, 2016.
5. Thomas Beyer, David W Townsend, Tony Brun, Paul E Kinahan, Martin Charron, Raymond Roddy, Jeff Jerin, John Young, Larry Byars, and Ronald Nutt.
A combined pet/ct scanner for clinical oncology.
Journal of nuclear medicine, 41(8):1369–1379, 2000.
6. David W Townsend, Jonathan PJ Carney, Jeffrey T Yap, and Nathan C Hall.

- Pet/ct today and tomorrow.
Journal of Nuclear Medicine, 45(1 suppl):4S–14S, 2004.
7. Zongwei Zhou, Md Mahfuzur Rahman Siddiquee, Nima Tajbakhsh, and Jianming Liang.
 Unet++: A nested u-net architecture for medical image segmentation.
 In *Deep Learning in Medical Image Analysis and Multimodal Learning for Clinical Decision Support: 4th International Workshop, DLMIA 2018, and 8th International Workshop, ML-CDS 2018, Held in Conjunction with MICCAI 2018, Granada, Spain, September 20, 2018, Proceedings 4*, pages 3–11. Springer, 2018.
 8. Fausto Milletari, Nassir Navab, and Seyed-Ahmad Ahmadi.
 V-net: Fully convolutional neural networks for volumetric medical image segmentation.
 In *2016 fourth international conference on 3D vision (3DV)*, pages 565–571. Ieee, 2016.
 9. Ali Hatamizadeh, Yucheng Tang, Vishwesh Nath, Dong Yang, Andriy Myronenko, Bennett Landman, Holger R Roth, and Daguang Xu.
 Unetr: Transformers for 3d medical image segmentation.
 In *Proceedings of the IEEE/CVF winter conference on applications of computer vision*, pages 574–584, 2022.
 10. Zaiwang Gu, Jun Cheng, Huazhu Fu, Kang Zhou, Huaying Hao, Yitian Zhao, Tianyang Zhang, Shenghua Gao, and Jiang Liu.
 Ce-net: Context encoder network for 2d medical image segmentation.
IEEE transactions on medical imaging, 38(10):2281–2292, 2019.
 11. Debesh Jha, Pia H Smedsrud, Michael A Riegler, Dag Johansen, Thomas De Lange, Pål Halvorsen, and Håvard D Johansen.
 Resunet++: An advanced architecture for medical image segmentation.
 In *2019 IEEE international symposium on multimedia (ISM)*, pages 225–2255. IEEE, 2019.
 12. Robert J Gillies, Paul E Kinahan, and Hedvig Hricak.
 Radiomics: images are more than pictures, they are data.
Radiology, 278(2):563–577, 2016.
 13. Chintan Parmar, Patrick Grossmann, Johan Bussink, Philippe Lambin, and Hugo JWL Aerts.
 Machine learning methods for quantitative radiomic biomarkers.
Scientific reports, 5(1):13087, 2015.
 14. Chih-Yang Hsu, Mike Doubrovina, Chia-Ho Hua, Omar Mohammed, Barry L Shulkin, Sue Kaste, Sara Federico, Monica Metzger, Matthew Krasin, Christopher Tinkle, et al.
 Radiomics features differentiate between normal and tumoral high-fdg uptake.
Scientific Reports, 8(1):3913, 2018.
 15. Marta Bogowicz, Stephanie Tanadini-Lang, Matthias Guckenberger, and Oliver Riesterer.
 Combined ct radiomics of primary tumor and metastatic lymph nodes improves prediction of loco-regional control in head and neck cancer.
Scientific reports, 9(1):15198, 2019.
 16. Jean-Emmanuel Bibault, Philippe Giraud, Martin Housset, Catherine Durdax, Julien Taieb, Anne Berger, Romain Coriat, Stanislas Chaussade, Bertrand Dousset, Bernard Nordlinger, et al.
 Deep learning and radiomics predict complete response after neo-adjuvant chemoradiation for locally advanced rectal cancer.
Scientific reports, 8(1):12611, 2018.
 17. Guangyao Wu, Arthur Jochems, Turkey Refaee, Abdalla Ibrahim, Chenggong Yan, Sebastian Sanduleanu, Henry C Woodruff, and Philippe Lambin.
 Structural and functional radiomics for lung cancer.
European Journal of Nuclear Medicine and Molecular Imaging, 48:3961–3974, 2021.
 18. Xiaonan Shao, Rong Niu, Xiaoliang Shao, Zhenxing Jiang, and Yuetao Wang.
 Value of 18f-fdg pet/ct-based radiomics model to distinguish the growth patterns of early invasive lung adenocarcinoma manifesting as ground-glass opacity nodules.
EJNMMI research, 10(1):1–12, 2020.
 19. Zhiguo Zhou, Kai Wang, Michael Folkert, Hui Liu, Steve Jiang, David Sher, and Jing Wang.
 Multifaceted radiomics for distant metastasis prediction in head & neck cancer.
Physics in Medicine & Biology, 65(15):155009, 2020.
 20. Matea Pavic, M Bogowicz, J Kraft, D Vuong, M Mayinger, SGC Kroeze, M Friess, T Frauenfelder, N Andratschke, M Huellner, et al.
 Fdg pet versus ct radiomics to predict outcome in malignant pleural mesothelioma patients.

- EJNMMI research*, 10(1):1–8, 2020.
21. Youcai Li, Yin Zhang, Qi Fang, Xiaoyao Zhang, Peng Hou, Hubing Wu, and Xinlu Wang.
Radiomics analysis of [18 f] fdg pet/ct for microvascular invasion and prognosis prediction in very-early-and early-stage hepatocellular carcinoma.
European journal of nuclear medicine and molecular imaging, 48:2599–2614, 2021.
 22. Yunming Xie, Hongguang Zhao, Yan Guo, Fanyang Meng, Xiangchun Liu, Yiyang Zhang, Xiaochen Huai, Qianting Wong, Yu Fu, and Huimao Zhang.
A pet/ct nomogram incorporating suvmax and ct radiomics for preoperative nodal staging in non-small cell lung cancer.
European radiology, 31:6030–6038, 2021.
 23. Kalevi Kairemo, S Cheenu Kappadath, Timo Joensuu, and Homer A Macapinlac.
A retrospective comparative study of sodium fluoride (naf-18)-pet/ct and fluorocholine (f-18-ch) pet/ct in the evaluation of skeletal metastases in metastatic prostate cancer using a volumetric 3-d radiomics analysis.
Diagnostics, 11(1):17, 2020.
 24. Ping Yin, Ning Mao, Chao Zhao, Jiangfen Wu, Lei Chen, and Nan Hong.
A triple-classification radiomics model for the differentiation of primary chordoma, giant cell tumor, and metastatic tumor of sacrum based on t2-weighted and contrast-enhanced t1-weighted mri.
Journal of Magnetic Resonance Imaging, 49(3):752–759, 2019.
 25. Hossein Naseri, Sonia Skamene, Marwan Tolba, Mame Daro Faye, Paul Ramia, Julia Khrguiian, Haley Patrick, Aixa X Andrade Hernandez, Marc David, and John Kildea.
Radiomics-based machine learning models to distinguish between metastatic and healthy bone using lesion-center-based geometric regions of interest.
Scientific Reports, 12(1):9866, 2022.
 26. Ning Lang, Yang Zhang, Enlong Zhang, Jiahui Zhang, Daniel Chow, Peter Chang, J Yu Hon, Huishu Yuan, and Min-Ying Su.
Differentiation of spinal metastases originated from lung and other cancers using radiomics and deep learning based on dce-mri.
Magnetic resonance imaging, 64:4–12, 2019.
 27. Laura Filograna, Jacopo Lenkowicz, Francesco Cellini, Nicola Dinapoli, Stefania Manfrida, Nicola Magarelli, Antonio Leone, Cesare Colosimo, and Vincenzo Valentini.
Identification of the most significant magnetic resonance imaging (mri) radiomic features in oncological patients with vertebral bone marrow metastatic disease: a feasibility study.
La radiologia medica, 124:50–57, 2019.
 28. Ricarda Hinzpeter, Livia Baumann, Roman Guggenberger, Martin Huellner, Hatem Alkadhi, and Bettina Baessler.
Radiomics for detecting prostate cancer bone metastases invisible in ct: a proof-of-concept study.
European Radiology, pages 1–10, 2022.
 29. Xin Fan, Han Zhang, Yuzhen Yin, Jiajia Zhang, Mengdie Yang, Shanshan Qin, Xiaoying Zhang, and Fei Yu.
Texture analysis of 18f-fdg pet/ct for differential diagnosis spinal metastases.
Frontiers in Medicine, 7:605746, 2021.
 30. Avi Ben-Cohen, Eyal Klang, Stephen P Raskin, Shelly Soffer, Simona Ben-Haim, Eli Konen, Michal Marianne Amitai, and Hayit Greenspan.
Cross-modality synthesis from ct to pet using fcnn and gan networks for improved automated lesion detection.
Engineering Applications of Artificial Intelligence, 78:186–194, 2019.
 31. Lei Bi, Jinman Kim, Ashnil Kumar, Dagan Feng, and Michael Fulham.
Synthesis of positron emission tomography (pet) images via multi-channel generative adversarial networks (gans).
In *Molecular Imaging, Reconstruction and Analysis of Moving Body Organs, and Stroke Imaging and Treatment: Fifth International Workshop, CMMI 2017, Second International Workshop, RAMBO 2017, and First International Workshop, SWITCH 2017, Held in Conjunction with MICCAI 2017, Québec City, QC, Canada, September 14, 2017, Proceedings 5*, pages 43–51. Springer, 2017.
 32. Martin Benning, Michael Möller, Raz Z Nossek, Martin Burger, Daniel Cremers, Guy Gilboa, and Carola-Bibiane Schönlieb.

- Nonlinear spectral image fusion.
In *Scale Space and Variational Methods in Computer Vision: 6th International Conference, SSVM 2017, Kolding, Denmark, June 4–8, 2017, Proceedings 6*, pages 41–53. Springer, 2017.
33. Leonie Zeune, Guus van Dalum, Leon WMM Terstappen, Stephan A van Gils, and Christoph Brune.
Multiscale segmentation via bregman distances and nonlinear spectral analysis.
SIAM journal on imaging sciences, 10(1):111–146, 2017.
 34. Marco Fumero, Michael Möller, and Emanuele Rodolà.
Nonlinear spectral geometry processing via the tv transform.
ACM Transactions on Graphics (TOG), 39(6):1–16, 2020.
 35. Ester Hait and Guy Gilboa.
Spectral total-variation local scale signatures for image manipulation and fusion.
IEEE Transactions on Image Processing, 28(2):880–895, 2018.
 36. Phu-Hung Dinh.
Combining spectral total variation with dynamic threshold neural p systems for medical image fusion.
Biomedical Signal Processing and Control, 80:104343, 2023.
 37. Giovanni Bellettini, Vicent Caselles, and Matteo Novaga.
The total variation flow in rn.
Journal of Differential Equations, 184(2):475–525, 2002.
 38. Tamara G Grossmann, Yury Korolev, Guy Gilboa, and Carola Schoenlieb.
Deeply learned spectral total variation decomposition.
Advances in Neural Information Processing Systems, 33:12115–12126, 2020.
 39. Tamara G Grossmann, Sören Dittmer, Yury Korolev, and Carola-Bibiane Schönlieb.
Unsupervised learning of the total variation flow.
arXiv preprint arXiv:2206.04406, 2022.
 40. Andreas Langer and Sara Behnamian.
Deeptv: A neural network approach for total variation minimization.
arXiv preprint arXiv:2409.05569, 2024.
 41. Pulkit Khandelwal, D Louis Collins, and Kaleem Siddiqi.
Spine and individual vertebrae segmentation in computed tomography images using geometric flows and shape priors.
Frontiers in Computer Science, 3:592296, 2021.
 42. Ross T Whitaker.
A level-set approach to 3d reconstruction from range data.
International journal of computer vision, 29:203–231, 1998.
 43. Jia Deng, Wei Dong, Richard Socher, Li-Jia Li, Kai Li, and Li Fei-Fei.
Imagenet: A large-scale hierarchical image database.
In *2009 IEEE conference on computer vision and pattern recognition*, pages 248–255. Ieee, 2009.
 44. Xueyan Mei, Zelong Liu, Philip M Robson, Brett Marinelli, Mingqian Huang, Amish Doshi, Adam Jacobi, Chendi Cao, Katherine E Link, Thomas Yang, et al.
Radimagenet: an open radiologic deep learning research dataset for effective transfer learning.
Radiology: Artificial Intelligence, 4(5):e210315, 2022.
 45. Joost JM Van Griethuysen, Andriy Fedorov, Chintan Parmar, Ahmed Hosny, Nicole Aucoin, Vivek Narayan, Regina GH Beets-Tan, Jean-Christophe Fillion-Robin, Steve Pieper, and Hugo JWL Aerts.
Computational radiomics system to decode the radiographic phenotype.
Cancer research, 77(21):e104–e107, 2017.
 46. Kaiming He, Xiangyu Zhang, Shaoqing Ren, and Jian Sun.
Identity mappings in deep residual networks.
In *Computer Vision—ECCV 2016: 14th European Conference, Amsterdam, The Netherlands, October 11–14, 2016, Proceedings, Part IV 14*, pages 630–645. Springer, 2016.